Science Robotics

robotics.sciencemag.org/cgi/content/full/2/11/eaao5619/DC1

Supplementary Materials for

A biologically inspired, flapping-wing, hybrid aerial-aquatic microrobot

Yufeng Chen,* Hongqiang Wang, E. Farrell Helbling, Noah T. Jafferis, Raphael T. Zufferey, Aaron Ong, Kevin Ma, Nicholas Gravish, Pakpong Chirarattananon, Mirko Kovac, Robert J. Wood*

*Corresponding author. Email: rjwood@eecs.harvard.edu (R.J.W.); yufengchen@seas.harvard.edu (Y.C.)

Published 25 October 2017, *Sci. Robot.* **2**, eaao5619 (2017)
DOI: 10.1126/scirobotics.aao5619

The PDF file includes:

Other Supplementary Material for this manuscript includes the following:
(available at robotics.sciencemag.org/cgi/content/full/2/11/eaao5619/DC1)

Movie S1 (.mp4 format). Demonstration of robot aerial hover.
Movie S2 (.mp4 format). Demonstration of robot air-water transition.
Movie S3 (.mp4 format). Demonstration of robot swimming and emergence of robot wing from the water surface.
Movie S4 (.mp4 format). Demonstration of robot impulsive takeoff and landing.
Movie S5 (.mp4 format). Comparison of robot underwater stability with different flapping frequencies.
Movie S6 (.mp4 format). Comparison between robot swimming experiment and simulation.
Movie S7 (.mp4 format). Measurement of surface tension force on a robot during water-to-air transition.
Movie S8 (.mp4 format). Comparison of robot takeoff with or without micro-openings on gas collection chamber.
Movie S9 (.mp4 format). Detonation pressure measurement and robot takeoff.

Supplementary Text

1. Electrolytic plates geometry and efficiency

We investigate electrolytic efficiency because the reaction is energetically costly. First, we estimate energy expenditure per takeoff assuming perfect efficiency. The volume of the gas collection chamber is 450 mm^3, which implies 300 mm^3 hydrogen and 150 mm^3 oxygen are produced. Assuming standard temperature and pressure, we estimate the electrolytic plates need to disassociate 1.3e-5 moles of water. The enthalpy of water electrolysis is 286 kJ/mol, which implies each takeoff consumes 3.8 J of energy.

Electrolysis reactions cannot achieve perfect efficiency due to over-potential. We can quantify the amount of energy spent by measuring current and integrating power expenditure over the reaction time: $E_{meas} = \int_0^T v(t)i(t)dt \approx V \cdot IT$, where V is the voltage input, I is the average current and T is the total reaction time. In this equation, the product IT is proportional to the number of disassociated electrons, which further relates to net gas volume. Hence, IT is a constant for any fixed chamber volume. This analysis suggests energy input is directly proportional to input voltage. The lower bound of input voltage is 1.23 V, which is the minimum reaction potential. While lowering electrolysis voltage improves efficiency, it reduces the average current and increases the total reaction time.

To reduce input voltage while maintaining average current, we reduce water resistance by improving plate geometry (*32*). Specifically, we fabricate 25 interdigitated electrolytic plates of varying plate finger width and gap (Fig. S1F). We vary the input voltage from 0 V to 10 V and measure the corresponding current for every device. Then we calculate the corresponding resistance through linear fitting. Fig. S1G shows the measured resistance as a function of plate width and gap. We observe that resistance increases as plate finger width or gap increases.

Resistance is proportional to the distance an electron travels in water, which is equal to the sum of plate width and gap. Fig. S1H shows a simple resistance model: $r = C(w + g)$. Here C is a fitted constant, w and g are plate finger width and gap, respectively. This model yields good qualitative agreement with our measurement. The most efficient plates have width and gap of 0.1 mm, and its measured resistance is 59 Ω.

Although plates with smaller width and gap are more efficient, they are harder to fabricate. We set both plate width and gap to 0.2 mm for takeoff experiments. The measured resistance of this device is 98 Ω, which is 66% larger than the most efficient plates. This design operates at 7.5 V and completely fills the gas collection chamber in 120 seconds. The total energy expenditure is 16 J, and the device efficiency is 23%. The energy density of lithium batteries is 1.8 J/mg, which implies that each takeoff will exhaust energy from approximately 10 mg of battery. The power consumption for robot hovering is 300 mW, which suggests that each water-air transition corresponds to an approximate flight time of 40 - 60 seconds.

2. Effect of micro-openings on gas capture

Gas produced by the electrolysis reaction needs to be captured by the chamber. Although there are circular micro-openings on its top plate, the chamber can still collect gas by utilizing surface tension effects (Fig. S4A). As oxyhydrogen is created, the surrounding water is displaced out of the chamber through the open chamber bottom. To prevent water from flowing through the micro-openings, hydrostatic pressure needs to be balanced by capillary pressure. The hydrostatic pressure is linearly proportional to the distance from the water surface. Capillary pressure is calculated using the Young-Laplace equation, which relates pressure to the micro-opening radius and the material contact angle with water. We impose a force balance and obtain the following equation: $\rho_w g h \pi r^2 = 2\pi r \gamma \cos\theta_C$, where h is the height of the gas collection chamber, r is the micro-opening radius, γ is the surface tension coefficient, and θ_C is the contact angle. We rearrange

this equation and obtain a relation between height h and micro-opening radius r: $h = \frac{2\gamma \cos\theta_C}{\rho_w g r}$. Fig. S4B shows this relation for the current chamber design.

This relation offers guidelines for robot design and fabrication. We can interpret h as the maximum height of the gas chamber. The chamber cannot capture additional gas if its chamber height exceeds h since gas will escape through the micro-openings. We can increase the maximum height h by increasing the fluid surface tension coefficient, reducing the contact angle, or reducing the opening radius. In our experiment the gas chamber height is 5.75 mm. According to the previous equation, it suggests that the opening radius to be smaller than 500 μm. Here we set the opening radius to 34 μm to satisfy this constraint. We choose the opening radius to be as small as possible such that less gas leaks from the chamber during the initial gas collection process.

3. Robot stability near the water surface

The robot needs to maintain upright stability as its wings gradually emerge from water. If the robot body tilts significantly in this process, gas leaks via the chamber's uncovered bottom face and the buoyant force decreases.

Surface tension forces destabilize the robot along the body pitch and roll axes. The definition of robot pitch, roll, and yaw axes is given in Fig. S11A**.** Fig. S5A illustrates body pitch instability in which the surface tension force creates a counter-clockwise torque. Gas leaks from the chamber's bottom face and the robot is unable to generate sufficient buoyancy force. Fig. S5B shows an image from a related experiment illustrating pitch instability. Pitch instability can be resolved by placing a balance beam along the pitch axis.

The robot is also unstable along the roll axis due to similar surface tension effects (Fig. S5C). Here one robot wing pushes through the water surface but the other one remains fully submerged (Fig. S5D). We place balance beams in both pitch and roll axes to resolve pitch and roll instability. The surface tension force on the balance beams stabilizes the robot while the buoyancy force pushes both wings out of the water (Fig. S5E). Fig. S5F shows successful wing water-air transition after installing balance beams.

4. Effect of micro-openings on takeoff

Micro-openings on the chamber top plate lower the detonation pressure. Robot takeoff experiments are expensive because large detonation pressures can lead to severe robot damage. We simplify takeoff experiments by replacing robot halves with dummy weights. We further replace titanium balance beams with carbon fiber ones due to ease of fabrication. The device in Fig. S6 weighs 170 mg and has an identical chamber as the real robot.

Fig. S6A illustrates device takeoff without micro-openings. Large detonation pressures crack the chamber's top plate and all balance beams break during takeoff. The vertical takeoff speed is 2.0 m/s. Fig. S6B shows device takeoff with micro-openings. The vertical takeoff speed reduces to 1.4 m/s and the chamber is undamaged. Fig. S6C shows a time image sequence of the same experiment during the early phase of takeoff. Water is ejected from the micro-openings within 0.5 ms of ignition. The openings release detonation energy and reduce takeoff speed.

We repeat the chamber explosion experiments five times. For the case of completely sealed chambers, there is noticeable damage in each experiment. In all five trials, the carbon fiber balance beams break in ways similar to the case shown in Fig. S6A. In two trials, the chamber's side walls are blown apart during takeoff. In the rest of the experiments, we observe cracks and deformation on the chamber's top plate and side walls. The sealed chambers cannot be reused after an explosion.

For the case of chambers with micro-openings, we observe significantly less damage. The chamber balance beams remain undamaged in three out of the five experiments. The chamber is undamaged in four out of the five experiments. There is one experiment where the chamber is slightly damaged; there is a small crack on the chamber's side piece and the local epoxy sealant is removed by the explosion.

The first two columns of Fig. S6, D and E compare the chamber's initial horizontal and vertical takeoff speeds. The red dots show the takeoff speed of each individual experiment and the blue circles and lines show the mean and standard deviation. The horizontal speed (Fig. S6D) is approximately six times smaller than the vertical takeoff speed (Fig. S6E). With the micro-openings, the chamber's mean vertical takeoff speed is reduced by 57%.

Next, we install chambers with micro-openings on a robot and perform five experiments. Here the balance beams are made of titanium T-beams. The robot remains undamaged in three out of the five trials. In one trial, the tabs of the titanium chamber top piece are detached from the side piece slots. The local epoxy sealant is removed by the explosion. In the other trial, one buoyant outrigger is blown away from the balance beam upon takeoff. In these two cases, the damage is minor and they can be easily repaired. Finally, we conduct one takeoff experiment using a robot with a sealed chamber. As described in the main text, the robot is severely damaged in the experiment. We do not repeat this experiment because robot and chamber fabrication is costly.

The last two columns of Fig. S6, D and E compare the robot's initial takeoff speed. Compared to the case with a sealed chamber, the mean horizontal and vertical speeds of the robot with chamber openings are reduced by 83% and 37%, respectively.

We further quantify the influence of micro-openings on detonation pressure. Unlike previous experiments, here we reinforce the sealed chamber with a 250 μm thick FR4 top plate so the chamber can survive the detonation. This extra reinforcement plate weighs 20 mg. We place a Kistler 601B1 pressure sensor beneath the robot chamber to measure pressure at the ignition location.

Fig. S7, A and B compare ignition pressure and takeoff velocity of robots with or without micro-openings. Measurements shown in Fig. S7, A and B resemble typical underwater explosion profiles in that a primary pressure peak is followed by an oscillatory tail (*33*). Fig. S7, A and B show that the presence of micro-openings reduces the maximum pressure by 3.4 times and increases the initial pressure pulse width by 39%.

We observe that the robot without micro-openings has a significantly lower takeoff speed despite having a higher maximum pressure (movie S9, and the red curves in Fig. S7, A and B). This observation differs from unreinforced explosion experiments in which the robot with a fully sealed chamber has a higher takeoff speed. In unreinforced explosion experiments, the detonation pressure cracks the fully sealed chamber and the cracks serve similar functions as the micro-openings.

Without cracks or micro-openings, the initial positive pressure pulse width decreases. Fig. S7, A and B mark four critical events along the pressure profile: ignition, start of pressure rise, pressure peak, and pressure drop. Fig. S7, C and D show the corresponding images of both experiments. The red circle in Fig. S7C shows that the chamber without micro-openings had not fully emerged from water surface when pressure fell negative. Consequently, the robot decelerates due to negative pressure caused by cavity contraction. In contrast, the red circle in Fig. S7D shows that the chamber with micro-openings completely exited the water surface before the pressure became negative. Consequently, cavity contraction has no effect on robot takeoff. In summary, the presence of micro-openings improves robot takeoff by reducing peak combustion pressure and increasing initial pressure pulse width.

We further relate robot takeoff velocity to the pressure measurements. We let m_r denote the robot mass,

p_w denote the momentum of the displaced water, v_{exit} denote the robot velocity after the robot completely exits the water surface and t_{exit} denotes the corresponding time. The impulse-momentum equation gives:

$$m_r\ v_{exit} + p_w = \int_o^{t_{exit}} \left(F_{expl} + F_{visc} + F_{drag} + F_{surf} + F_g \right) dt\ , \tag{2}$$

where the total force is contributed by the explosion, viscous drag, pressure drag, surface tension, and the robot's weight. Each component is calculated as:

$$F_{expl} = PA_t\ , \tag{3}$$

$$F_{visc} = -A_w \mu u \frac{1}{\sqrt{\pi \nu t}}\ , \tag{4}$$

$$F_{drag} = -\frac{1}{2} \rho C_D u \|u\| A_t\ , \tag{5}$$

$$F_{surf} = -2\gamma L\ , \tag{6}$$

$$F_g = -mg\ , \tag{7}$$

Here P and u are instantaneous pressure and velocity. The values of other terms are documented in table S2. By comparison, F_{expl} is on the order of several Newtons within the first millisecond and it dominates all other components so that the takeoff velocity can be approximated as:

$$v_{exit} \approx \frac{1}{m_r} \left(\int_o^{t_{exit}} F_{expl} dt - p_w \right). \tag{8}$$

Based on the high-speed videos, we estimate t_{exit} = 1.1 ms and 2.3 ms for the robot with or without chamber micro-openings, respectively. The corresponding robot takeoff velocities are 3 m/s and 1 m/s, respectively. Having measured other terms in the previous equation, we solve for the momentum of the displaced water. We estimate p_w = 2 mN s and 7 mN s for the case with or without micro-openings. In both cases the robot takeoff momentum is within 10% of the net impulse. This result shows that most of the impulse is absorbed by the water.

5. Derivation of dynamical model

5.1. Notations

We use the following notations for the derivations:

- We use bold letters to denote vector quantities and hat to denote unit vectors $\mathbf{0}$ denotes a vector of all 0 s. For the special unit vector that's parallel to a particular coordinate axis, we write the vector as $\mathbf{e_i}$ without a hat. It means the vector is 1 at the i^{th} entry and 0 everywhere else.
- We use upper case letters to represent matrix quantities. Specifically, we use R to denote a 3×3 rotation matrix.

- For vectors $\mathbf{v} \in R^3$, $\mathbf{a} \in R^3$, we let $S_{\mathbf{v}}$ denote the skew symmetric matrix generated by $\mathbf{v}$ such that $S_{\mathbf{v}}\mathbf{a} = \mathbf{v} \times \mathbf{a}$.

5.2 Robot dynamical model

We formulate a time varying model that has 10 degrees of freedom. The robot body has six translational and rotational degrees of freedom denoted by x, y, z, ϕ, θ, and ψ. Here x, y, z, are the translational degrees of freedom and ϕ, θ, and ψ are Euler angles following the roll, pitch, and yaw convention. Fig. S11A defines the robot body and wing coordinate axes. The robot wing kinematics each have two degrees of freedom relative to the robot body for a total of four degrees of freedom corresponding to the robot's left and right wings. Here α_i and β_i denote wing stroke and pitch angle, respectively. The subscript i distinguishes the left and the right wing. These ten generalized coordinates are defined as a column vector:

$$\mathbf{q} = [x, y, z, \phi, \theta, \psi, \alpha_r, \beta_r, \alpha_l, \beta_l]^T \tag{9}$$

Here we denote right and left wing by the abbreviations r and l, respectively.

5.2.1 Rigid body dynamics

We adopt the matrix form of Lagrangian mechanics to derive the equation of motion (*34*):

$$D(\mathbf{q})\ddot{\mathbf{q}} + C(\mathbf{q}, \dot{\mathbf{q}})\dot{\mathbf{q}} + \mathbf{g}(\mathbf{q}) = \boldsymbol{\tau}. \tag{10}$$

The inertia matrix D is given by the sum of contributions from body, right and left wing:

$$D = \sum_{i \in \{\mathrm{b,r,l}\}} \{J_{v,i}^T R_i M R_i^T J_{v,i} + J_{w,i}^T R_i I R_i^T J_{w,i}\}, \tag{11}$$

where M and I are the mass and moment of inertia matrix, respectively. Here mass is a tensor quantity to account for geometry-dependent added mass effects. R_i is the corresponding rotation matrix from the center of mass reference frame to the inertial system. $J_{v,i}$ and $J_{w,i}$ are velocity and angular velocity Jacobians. The Christophol matrix elements are obtained from the partial differentials of the inertia matrix:

$$C_{kj} = \sum_{i=1}^{n} C_{ijk}(\mathbf{q})\dot{q}_i = \sum_{i=1}^{n} \frac{1}{2}\{\frac{\partial D_{kj}}{\partial q_j} + \frac{\partial D_{ki}}{\partial q_j} - \frac{\partial D_{ij}}{\partial q_k}\}\dot{q}_i. \tag{12}$$

The jth component of the gravity vector is given by:

$$g_j = \frac{\partial P}{\partial q_j}, \tag{13}$$

where P is the total potential energy. The generalized force vector $\boldsymbol{\tau}$ is given by the matrix product of the partial displacement matrix and the external force vector. The dimensionalities of these quantities are given by: $D \in R^{10\times10}$, $C \in R^{10\times10}$, $g \in R^{10\times1}$, $\boldsymbol{\tau} \in R^{10\times1}$. The equations of motion form a system of coupled ordinary differential equations. We solve this system numerically through the matlab function ode45.

Next, we derive the velocity Jacobians and angular velocity Jacobians of the robot body, its right and left wing. The body velocity Jacobian $J_{v,b}$ transforms velocities with respect to the generalized coordinate to velocities with respect to the inertial coordinate. Here we have $J_{v,b} \in R^{3\times 10}$ and it is given by:

$$J_{v,b} = \begin{pmatrix} | & | & | & | & | & | & | & | & | & | \\ \mathbf{e_1} & \mathbf{e_2} & \mathbf{e_3} & \mathbf{0} & \mathbf{0} & \mathbf{0} & \mathbf{0} & \mathbf{0} & \mathbf{0} & \mathbf{0} \\ | & | & | & | & | & | & | & | & | & | \end{pmatrix}, \tag{14}$$

The body angular velocity Jacobian is given by

$$J_{w,b} = \begin{pmatrix} | & | & | & | & | & | & | & | & | & | \\ \mathbf{0} & \mathbf{0} & \mathbf{0} & R_\psi R_\theta \mathbf{e_1} & R_\psi \mathbf{e_2} & \mathbf{e_3} & \mathbf{0} & \mathbf{0} & \mathbf{0} & \mathbf{0} \\ | & | & | & | & | & | & | & | & | & | \end{pmatrix}, \tag{15}$$

where R_ψ and R_θ are rotation matrices with respect to the ψ and θ axes. In the next sections we will use the rotation matrices R_ψ, $R_{\alpha r}$, $R_{\alpha l}$, $R_{\beta r}$, and $R_{\beta l}$. These are rotations with respect to the axes defined in Fig. S11B.

5.2.2 Body and wing displacement vectors

The right and left wing velocity and angular velocity Jacobians contain a number of displacement vectors that define the distance between the robot center of mass, wing root, and wing center of mass. These vectors are defined as:

- $\mathbf{d}_{rb}$: displacement from the body center of mass to the right wing center of mass
- $\mathbf{d}_{lb}$: displacement from the body center of mass to the left wing center of mass
- $\mathbf{d}_{rw}$: displacement from the right wing root to the right wing center of mass
- $\mathbf{d}_{lw}$: displacement from the left wing root to the left wing center of mass

These displacement vectors can be calculated from a sequence of translations and rotations from the default robot configuration. Let $\mathbf{r}_{rb}$, $\mathbf{r}_{lb}$, $\mathbf{r}_{rw}$, and $\mathbf{r}_{lw}$ be the corresponding robot parameters in the fixed frame. The transformation is given by:

$$\mathbf{d}_{rb} = R_b(\mathbf{r}_{rb} - \mathbf{r}_{rw}) + R_b R_{\alpha r} R_{\beta r} \mathbf{r}_{rw}, \tag{16}$$

$$\mathbf{d}_{lb} = R_b(\mathbf{r}_{lb} - \mathbf{r}_{lw}) + R_b R_f R_{\alpha l} R_{\beta l} \mathbf{r}_{lw}, \tag{17}$$

$$\mathbf{d}_{rw} = R_b R_{\alpha r} R_{\beta r} \mathbf{r}_{rw}, \tag{18}$$

$$\mathbf{d}_{lw} = R_b R_f R_{\alpha l} R_{\beta l} \mathbf{r}_{lw}, \tag{19}$$

where R_b is the body rotation matrix:

$$R_b = R_\psi R_\theta R_\phi. \tag{20}$$

The rotation matrix R_f accounts for the 180° rotation between the left wing coordinate and the body coordinate.

5.2.3 Jacobian matrices of the right wing

Fig. S11A shows the coordinate definition of the right wing with respect to the body frame. The wing rotates with respect to the stroke axis z_r and then the pitch axis y_r. The cumulative rotation matrix is given by

$$R_r = R_b R_{\alpha r} R_{\beta r}, \tag{21}$$

The right wing velocity Jacobian is given by

$$J_{v,r} = \begin{pmatrix} | & | & | & | & | & | & | & | & | & | \\ \mathbf{e}_1 & \mathbf{e}_2 & \mathbf{e}_3 & R_\psi R_\theta S_{\mathbf{e}_1} \mathbf{d}_{rb} & R_\psi S_{\mathbf{e}_2} \mathbf{d}_{rb} & S_{\mathbf{e}_3} \mathbf{d}_{rb} & R_b S_{\mathbf{e}_3} \mathbf{d}_{rw} & R_b R_{\alpha r} S_{\mathbf{e}_2} \mathbf{d}_{rw} & \mathbf{0} & \mathbf{0} \\ | & | & | & | & | & | & | & | & | & | \end{pmatrix}. \tag{22}$$

The right wing angular velocity Jacobian is given by

$$J_{w,r} = \begin{pmatrix} | & | & | & | & | & | & | & | & | & | \\ \mathbf{0} & \mathbf{0} & \mathbf{0} & R_\psi R_\theta \mathbf{e}_1 & R_\psi \mathbf{e}_2 & \mathbf{e}_3 & R_b \mathbf{e}_3 & R_b R_{\alpha r} \mathbf{e}_2 & \mathbf{0} & \mathbf{0} \\ | & | & | & | & | & | & | & | & | & | \end{pmatrix}. \tag{23}$$

5.2.4 Jacobian matrices of the left wing

Fig. S10A also shows the coordinate definition of the left wing with respect to the body frame. The left wing rotates with respect to the stroke axis z_l and then the pitch axis y_l. The cumulative rotation matrix is given by:

$$R_l = R_b R_f R_{\alpha l} R_{\beta l}. \tag{24}$$

The left wing velocity Jacobian is given by

$$J_{v,l} = \begin{pmatrix} | & | & | & | & | & | & | & | & | & | \\ \mathbf{e}_1 & \mathbf{e}_2 & \mathbf{e}_3 & R_\psi R_\theta S_{\mathbf{e}_1} \mathbf{d}_{lb} & R_\psi S_{\mathbf{e}_2} \mathbf{d}_{lb} & S_{\mathbf{e}_3} \mathbf{d}_{lb} & \mathbf{0} & \mathbf{0} & R_b R_{cf} S_{\mathbf{e}_3} \mathbf{d}_{lw} & R_b R_{cf} R_{\alpha l} S_{\mathbf{e}_2} \mathbf{d}_{lw} \\ | & | & | & | & | & | & | & | & | & | \end{pmatrix}, \tag{25}$$

The left wing angular velocity Jacobian is given by

$$J_{w,l} = \begin{pmatrix} | & | & | & | & | & | & | & | & | & | \\ \mathbf{0} & \mathbf{0} & \mathbf{0} & R_\psi R_\theta \mathbf{e}_1 & R_\psi \mathbf{e}_2 & \mathbf{e}_3 & \mathbf{0} & \mathbf{0} & R_b R_{cf} \mathbf{e}_3 & R_b R_{cf} R_{\alpha l} \mathbf{e}_2 \\ | & | & | & | & | & | & | & | & | & | \end{pmatrix}. \tag{26}$$

5.3 A time varying aerodynamic model

Here we generalize a previous quasi-steady blade element model (*35*) to account for body movement and

rotation. We aim to quantify the influence of robot kinematic parameters on swimming stability and speed.

In equation 10 the generalized force $\boldsymbol{\tau}$ relates to net external force, which consists of aerodynamic forces, flexure viscoelastic forces, and actuator driving forces:

$$\mathbf{F}_{ext} = \mathbf{F}_{aero} + \mathbf{F}_{flexure} + \mathbf{F}_{act}\,. \tag{27}$$

The aerodynamic force consists of contributions from the robot body and left and right wings. We describe the modeling of these external forces in the following sections.

5.3.1 Aerodynamic model of the robot body

Fig. S11C illustrates the robot body and wing centers of mass, and the corresponding aerodynamic forces. First, we consider the drag force on the robot body. Since the body center of mass does not coincide with its geometric center, we separately model the damping force and torque with respect to its center of mass.

The force on the robot body is predominately contributed by pressure because the corresponding Reynolds number is approximately 100. The drag force has quadratic dependence on body velocity:

$$\mathbf{F}_d = -\frac{1}{2}\rho C_d S_\perp \| \mathbf{v}_b \| \mathbf{v}_b\,, \tag{28}$$

where $\mathbf{v}_b$ is the instantaneous body velocity and $S_\perp$ is the frontal area normal to $\mathbf{v}_b$. The damping torque with respect to the body center of mass is given by

$$\boldsymbol{\Gamma}_d = -\frac{1}{2} C_\Gamma \rho r S_W^2 \| \boldsymbol{\omega} \| \boldsymbol{\omega}\,, \tag{29}$$

where $\boldsymbol{\omega}$ is the instantaneous angular velocity, S_W is the total wetted area, and r is the mean moment arm. C_d and C_Γ are the body drag and torque coefficients.

Since water density is approximately 900 times that of air, it is important to consider buoyancy and added mass effects for aquatic locomotion. Buoyancy accounts for nearly 25% of the robot weight. Here the buoyancy force is given by:

$$\mathbf{F}_{b,b} = \rho g V_{disp} \hat{\mathbf{z}}\,, \tag{30}$$

where V_{disp} is the volume displaced by the robot body.

Added mass effects arise because a moving robot body accelerates the nearby fluid. Specifically, this term depends on body surface area and fluid density. With respect to the inertial frame, we model added mass contribution as

$$M_{add} = \begin{pmatrix} \rho l S_x & 0 & 0 \\ 0 & \rho l S_y & 0 \\ 0 & 0 & \rho l S_z \end{pmatrix}, \tag{31}$$

where S_x, S_y and S_z are the corresponding frontal areas, ρ is the fluid density and l is a length scale.

l is a fitting parameter and we set it to be the robot width.

5.3.2 Blade element quasi-steady method

We adopt the classical quasi-steady blade element model and account for wing root movement from body motions. Following the blade element approach, we divide each wing into N chordwise panels and approximate each panel as translating on a 2D plane. Fig. S11D illustrates the translating and pitching motion of a chordwise panel. The instantaneous stroke plane is not orthogonal to the $\mathbf{z}$ axis due to robot oscillation.

First, we calculate each panel's instantaneous leading edge velocity using the wing velocity Jacobian:

$$\mathbf{v}_{le} = J_v \dot{\mathbf{q}}, \tag{32}$$

where $\mathbf{v}_{le}$ denotes the leading edge velocity. Next, we compute the normalized wing chord vector $\hat{\mathbf{c}}$ using rotation matrices derived from the previous chapter. The panel angle of attack is given by

$$AoA = \cos^{-1}(\hat{\mathbf{c}} \cdot \hat{\mathbf{v}}_{\perp}), \tag{33}$$

where $\hat{\mathbf{v}}_{\perp}$ is the normalized component of $\mathbf{v}_{le}$ orthogonal to the wing span. Given the local angle of attack, we compute local lift and drag coefficients following Dickinson's formula (*15*):

$$C_L = C_{L0} \sin 2AoA, \tag{34}$$

$$C_D = \frac{C_{D0} + C_{Dmax}}{2} - \frac{C_{Dmax} - C_{D0}}{2} \cos 2AoA, \tag{35}$$

where the coefficients are given by $C_{L0} = 1.8,\ C_{L0} = 1.8,\ C_{D0} = 0.4,$ and $C_{Dmax} = 3.4.$ Then we compute the direction of the lift and drag forces on the local panel:

$$\hat{\mathbf{f}}_L = \hat{\mathbf{w}}_{z,b}, \tag{36}$$

$$\hat{\mathbf{f}}_D = -\hat{\mathbf{v}}_{\perp}. \tag{37}$$

Here $\hat{\mathbf{w}}_{z,b}$ is the unit normal vector of the instantaneous stroke plane. These definitions are adopted from the aeromechanical model developed by Whitney et al (*35*). Finally, we compute the total lift and drag forces on the wing by summing the contribution from each panel:

$$\mathbf{F}_L = \frac{1}{2}\rho \sum_{i=1}^{N} C_L v_{\perp}^2 c(r_i) \hat{\mathbf{f}}_L \delta r, \tag{38}$$

$$\mathbf{F}_D = \frac{1}{2}\rho \sum_{i=1}^{N} C_D v_{\perp}^2 c(r_i) \hat{\mathbf{f}}_D \delta r. \tag{39}$$

Here $c(r_i)$ represents the local chord length of the i^{th} panel. The aerodynamic force contribution from the left and the right wing can be separately computed through invoking equations 38 and 39. We do not include

contribution from rotational circulation and added mass because their force coefficients are not quantified in previous studies. Inclusion of these terms may lead to unnecessary over-fitting.

The aerodynamic lift and drag forces, together with other external forces, need to be projected onto the generalized coordinates to obtain the generalized forces. The j^{th} component of the generalized force $\boldsymbol{\tau}$ can be calculated as:

$$\tau_j = \sum_k \mathbf{f}_{ext,k} \cdot \frac{\partial \mathbf{x}_k}{\partial q_j}, \tag{40}$$

where $\mathbf{x}_k$ is the center of pressure location of the k^{th} panel, and $\mathbf{f}_{ext,k}$ is the total external force on the k^{th} panel. To evaluate this equation, we need to estimate the center of pressure for each wing panel and integrate across the wing span. The center of pressure location can be computed given the local wing chord and a non-dimensionalized center of pressure r_{cop}. The relationship between r_{cop} and angle of attack is given in a previous study (*21*):

$$r_{cop} = 0.25 + 0.25 \times \frac{1}{1 + \exp(\gamma(1 - \frac{4}{\pi} AoA))}. \tag{41}$$

Here γ is a positive fitting parameter related to the wing geometry.

While the generalized force vector can be computed easily through equation 40, it does not offer a straightforward physical interpretation. The torque on the robot center of mass due to the fluid forces on the wing is given by:

$$\boldsymbol{\Gamma} = \frac{1}{2}\rho \sum_{i=1}^{N} \mathbf{r}_{p,i} \times \left(C_L \hat{\mathbf{f}}_L + C_D \hat{\mathbf{f}}_D \right) \| v_\perp \|^2 \, c(r_i) \delta r, \tag{42}$$

where $\mathbf{r}_{p,i}$ is the displacement from robot center of mass to the local center of pressure.

5.4 Forces from wing flexures and actuators

We model the wing flexure as a torsional spring with viscous damping. The torques exerted by the wing hinges along wing pitch axes are given by:

$$\tau_{\beta r} = -K_h \beta_r - D_h \dot{\beta}_r, \tag{43}$$

$$\tau_{\beta l} = -K_h \beta_l - D_h \dot{\beta}_l, \tag{44}$$

where K_h is the stiffness and D_h is the viscoelastic damping. Both parameters are dependent on the wing hinge geometry.

The piezoelectric actuator and robot transmission can be modeled as a sinusoidal torque source (26). The driving frequency and torque amplitude depend on the input electric signal. The input torque along the wing stroke axes are given by:

$$\tau_{\alpha r,act} = A_r \cos(2\pi ft). \tag{45}$$

$$\tau_{\alpha l,act} = A_l \cos(2\pi ft). \tag{46}$$

The robot transmission also exerts restoring and damping torque along the stroke axes:

$$\tau_{\alpha r,trans} = -K_t \alpha_r - D_t \dot{\alpha}_r, \tag{47}$$

$$\tau_{\alpha l,trans} = -K_t \alpha_l - D_t \dot{\alpha}_l, \tag{48}$$

where K_t and D_t are robot transmission stiffness and visoelastic damping coefficients.

6. Robot tracking

The recorded swimming videos show noticeable body pitching during robot locomotion. Here we quantify the amplitude of body pitching through post-processing the videos. We manually select two images of maximum body pitch in opposite directions. A number of tracking points are manually labeled given the recorded images. These are the 2D projection of specific reference points onto the camera image plane. Since there is an accurate geometrical model of the robot, we can estimate robot orientation by solving a constrained optimization problem. Specifically, the problem can be formulated as:

$$\arg\min_{\psi,\theta,\phi} \sum_i || R_{(1:2,:)}(\psi,\theta,\phi)\mathbf{s}_i - \mathbf{r}_i ||_2, \tag{49}$$

where $R_{(1:2,:)} \in R^{2\times 3}$ is the top two rows of the rotation matrix:

$$R = R_\psi R_\theta R_\phi. \tag{50}$$

$\mathbf{s}_i \in R^3$ is the displacement of the i^{th} reference point with respect to the robot center of mass, and $\mathbf{r}_i \in R^2$ is the corresponding measured location on the image. Here the measured location $\mathbf{r}_i$ can be calculated from the pixel values $\mathbf{p}_i$ through subtracting the centroid pixel values and then scaling by the appropriate length scale. This simple operation is given by

$$\mathbf{r}_i = s(\mathbf{p}_i - \mathbf{x}_c), \tag{51}$$

The robot centroid $\mathbf{x}_c$ is identified manually and the scaling constant s is obtained by measuring the aquarium dimensions from the image.

Equation 49 is solved using matlab's constrained optimization function *fmincon*. We impose constraints on the rotation angles such that $-\pi \le \phi,\theta,\psi \le \pi$. Fig. S11E labels the robot center of mass and several tracking points. Fig. S11F shows the numerical solution of the robot model projected onto the image plane.

7. Simplified model of robot passive upright stability

7.1 Passive upright stability during unpowered freefall

As we have discussed in the main text and the supplement, the robot is passively upright stable during unpowered freefall because its center of mass is lower than its center of pressure. This is a well-known fact in flight vehicle design. Here we give a simple proof.

We define the robot as passively upright stable if it can recover from small perturbations in the body pitch or roll axes. Intuitively, the drag force that acts above the center of mass gives a restoring torque that stabilizes the robot during freefall. Since the stability conditions for the pitch and roll axes are very similar, we give a simple derivation for the pitch axes stability condition. Fig. S12A illustrates the free body diagram of the robot during freefall. Using the Lagrangian formulation, we can write out the equation of motion during freefall:

$$I\ddot{\theta} = -c_1\dot{z}^2 r\sin\theta - c_2\left|\dot{\theta}\right|\dot{\theta}\,, \tag{52}$$

Here, I is the robot pitch-wise moment of inertia, and c_1 and c_2 are positive damping coefficients. The moment arm r is the distance between robot center of mass and its center of pressure. The variables θ and z are the body pitch and vertical descent motion, respectively. For a small angle θ, we linearize the equation as:

$$I\ddot{\theta} = -c_1\dot{z}^2 r\theta - c_2\left|\dot{\theta}_0\right|\dot{\theta}\,, \tag{53}$$

For simplicity, we first assume that $\dot{z}$ is a constant that equals the terminal velocity. Based on this assumption, we can define two positive constants $\alpha_1 = c_1\dot{z}^2 r$, and $\alpha_2 = c_2\dot{\theta}_0$. Equation 53 can be re-written as:

$$I\ddot{\theta} + \alpha_1\theta + \alpha_2\ddot{\theta} = 0\,, \tag{54}$$

We can show this dynamical system is stable by finding a Lyapunov function V and showing its derivative is strictly negative. Here we can let:

$$V = \frac{1}{2}I\dot{\theta}^2 + \frac{1}{2}\alpha_1\theta^2\,, \tag{55}$$

Taking the derivative and substituting equation (54) we find that:

$$\dot{V} = -\alpha_1\dot{\theta}^2 \le 0\,. \tag{56}$$

This derivation shows the system is stable. Furthermore, the simplification that $\dot{z}$ is a constant can be relaxed in a slightly more involved derivation. In the early part of the free fall, we can model the motion as $\dot{z} = -gt$. Consequently, equation 54 becomes a time dependent linear system:

$$\ddot{\theta} + a\dot{\theta} + bt^2\theta = 0\,, \tag{57}$$

where a and b are two positive constants. This equation can be solved analytically through series expansion. The general solution is:

$$\theta(t) = e^{-0.5t(a+i\sqrt{b}t)}\left(C_1 F_1^1\left(\frac{1}{4} - \frac{ia^2}{16\sqrt{b}}, \frac{1}{2}, i\sqrt{b}t\right) + C_2 F_1^1\left(\frac{3}{4} + \frac{ia^2}{16\sqrt{b}}, \frac{3}{4}, i\sqrt{b}t\right)\right). \tag{58}$$

Here F_1^1 is the hypergeometric function, C_1 and C_2 are two coefficients depending on the initial condition. Note that the third parameter in both hypergeometric functions is imaginary, hence that part is oscillatory.

Since a and b are positive, this solution is dominated by the exponential decay. Consequently, the angular deviation gradually approaches 0. The derivation for the roll axis stability is nearly identical. This shows that the robot remains passively upright during landing.

7.2 Passive upright stability during open-loop swimming

Through experiments and simulations, we find that when the robot operates at appropriate frequencies, it is passively upright stable during swimming. This is an important and unintuitive finding. It is practically important because our motion tracking system does not operate in water due to refraction of the infrared illumination. Consequently, closed-loop feedback control is not possible with the existing setup. Therefore, the robot needs to be stable when driven open-loop. This result is unintuitive because the robot is intrinsically unstable when flying in air. It requires closed-loop feedback control or passive dampers for stability. In this section, we show that passive dampers are not needed if the driving frequency is chosen appropriately.

We say that the robot is passive upright stable if it can recover from small perturbation from its roll and pitch axes. In our simulation, the robot is unstable if any of the two conditions are violated:

1. The maximum pitch or roll amplitudes must be smaller than 90°.
2. The robot center of mass must ascend upward with a positive mean speed.

The first condition ensures the robot does not tip over and swim downward. The second condition ensures the robot can lift off from underwater surfaces. Otherwise, it rocks back and forth. In our experiments, a robot that cannot lift off eventually tips over because its legs collide with the ground. Quantifying the stability condition requires a dynamical model that includes body-wing coupling and fluid drag on the robot body. Details about the full model derivation are given in the supplemental materials, section 5. Comparison of the full model with experiments is shown in Fig. 3. Here, we describe a simplified model that gives intuition on why the robot can be stable in water. This model aims to illustrate the trend of decreasing body pitch as the flapping frequency increases by considering body-wing coupling and fluid drag on the robot body. It does not give a proof of swimming stability.

Compared to flying in air, the robot experiences greater body-wing coupling and larger drag on the robot body when in water. These factors are crucial for stability. In air, the robot body experiences negligible oscillations so the aerodynamic damping on the robot body is very small. In water, the robot experiences larger oscillations and the water drag is much larger because the density of water is much higher. In addition, the body oscillation causes the wing root to become non-stationary and this coupling can influence stability. Fig. S12B shows a free body diagram and derives a simplified model for robot pitch.

In Fig. S12B, the drag force from the wing (F_W) destabilizes the robot. The first stabilizing factor is the body drag (F_B):

$$F_B = \frac{1}{2}\rho_w C_{D,B} S|u|u = \frac{1}{2}\rho_w \tilde{C}_{D,B} S^2 \left|\dot{\theta}\right|\dot{\theta}. \tag{59}$$

Here ρ_w is the density of water, $C_{D,B}$ is the drag coefficient of the robot body, S is the body surface area, and u is the body motion. We can rewrite this equation in terms of the pitch motion $\dot{\theta}$ and define a new drag coefficient $\tilde{C}_{D,B}$. This body drag contribution is much larger than it is in air because $\rho_w >> \rho_{air}$. This term alone cannot stabilize the robot – it delays the transition to tipping over.

Fig. S12C illustrates the second factor – the coupling between the robot body and the wing. When the wing moves at a large velocity, the body rotates at a large velocity in the opposing direction. This body movement effectively slows down the robot wing speed and reduces the drag force. To capture this effect, we approximate the drag force as:

$$F_W = \frac{1}{2}\rho_w C_D S_0 \left|R\dot{\alpha} + R'\dot{\theta}\right|(R\dot{\alpha} + R'\dot{\theta}), \tag{60}$$

where F_W is drag force on the wing, R is the distance from wing root to a local wing chord, R' is the distance from robot center of mass to the local wing chord, $\dot{\alpha}$ is the wing stroke speed and $\dot{\theta}$ is the body pitching speed. Instead of integrating along the wing span, we make an approximation by setting R and R' to the wing span and mean wing chord length. This simple model ignores wing shape and passive pitching influence on the drag coefficient. In this equation, the wing stroke motion α is the driving term:

$$\alpha = \alpha_0 \sin(2\pi ft). \tag{61}$$

Since the robot center of mass is lower than its center of pressure, buoyancy force creates a restoring torque: $\tau_B = F_{b,b} l \sin\theta$, where $F_{b,b}$ is the buoyancy force and it accounts for 25% of the robot weight. The symbol l is the distance from the robot center of mass to its center of pressure. Finally, we introduce a constant torque offset that is the result of manufacturing imprecision. We let τ_o denote a constant pitch disturbance.

In summary, the differential equation for swimming stability is given by:

$$A_0\ddot{\theta} + A_1\left|R\dot{\alpha} + R'\dot{\theta}\right|(R\dot{\alpha} + R'\dot{\theta}) + A_2\left|\dot{\theta}\right|\dot{\theta} + F_{b,b} l \sin\theta + \tau_0 = 0. \tag{62}$$

Here the parameters A_o, A_1, A_2, $F_{b,b}$, l, τ_o are coefficients associated with the robot geometry, inertia, and disturbance. We set the parameters to be $A_o = 1\times10^{-9}$ kgm^2, $A_1 = 2\times10^{-4}$ kg, $A_2 = 5\times10^{-8}$ kgm^2, $F_{b,b} = 0.2$ mN, $l = 2\times10^{-3}$ m and $\tau_o = 1\times10^{-7}$ Nm. Fig. S12, D and E compare two sample simulations, one at 5 Hz (red) and one at 10 Hz (green). The pitch amplitude is reduced by a factor of three when the flapping frequency reduces from 10 Hz to 5 Hz. Fig. S12F further shows that pitch amplitude (solid line) decreases monotonically as flapping frequency increases. Furthermore, due to the bias torque disturbance, the simulations show that there is a non-zero mean pitch offset (dotted line). The mean pitch bias also decreases as flapping frequency increases. This simple model illustrates that body pitching amplitude and pitch offset decrease as flapping frequency increases. While it is not a proof for swimming stability, it gives intuition on the contribution from the body damping and body-wing coupling.

Supplementary figure

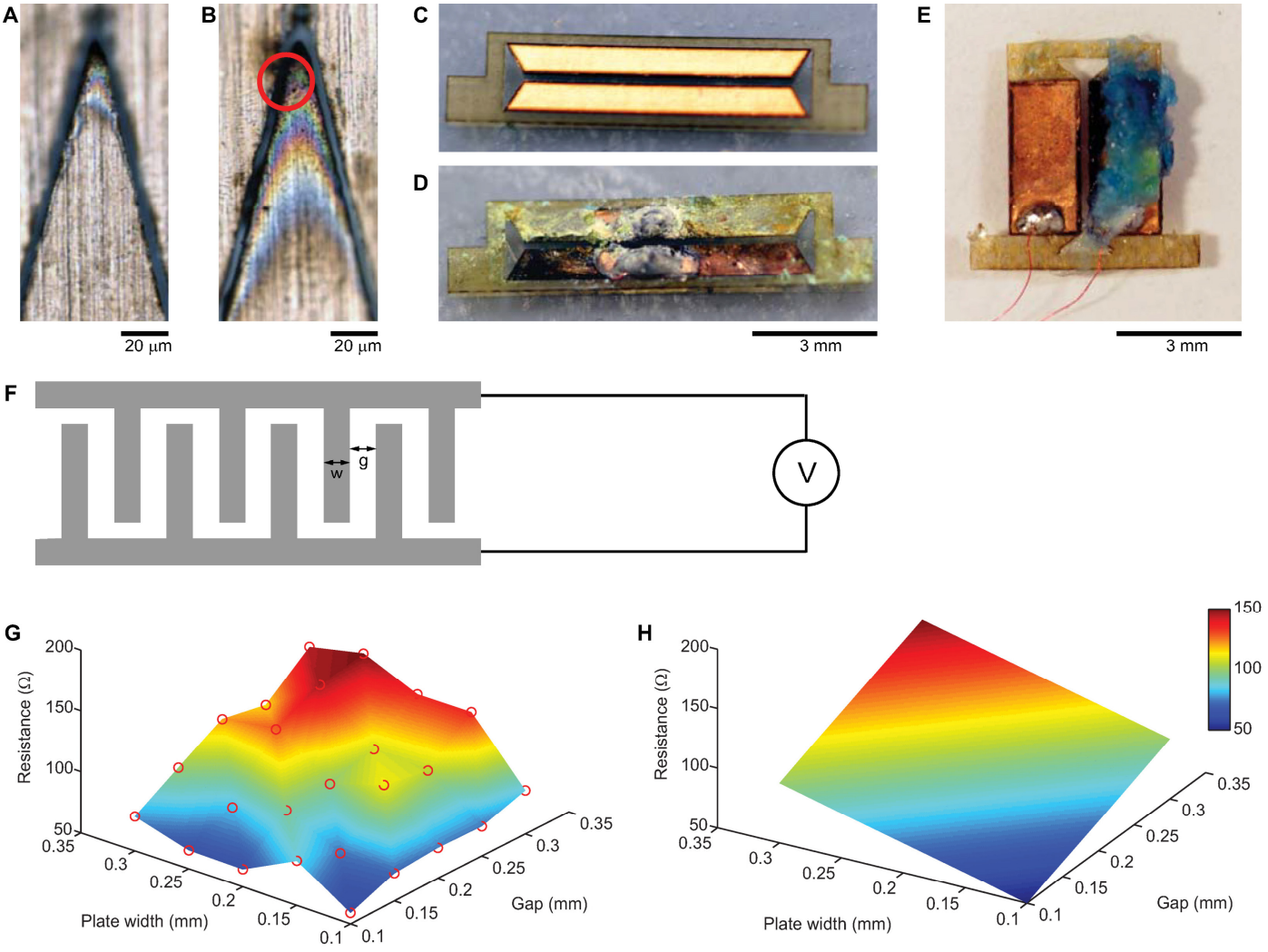

Fig. S1. Material selection of sparker and electrolytic plates, and plate geometry influence on water resistance during electrolysis. (A) A new stainless steel sparker tip. **(B)** A shorted stainless steel sparker tip after three ignitions. The sparker tip changes color due to the heat associated with sparking. The red circle highlights the shorted region. **(C)** A new pair of copper electrolytic plates. **(D)** A pair of electrolytic plates after 120 seconds of reaction. Most of the copper on the anode disappears. **(E)** Copper oxide growth on the anode. **(F)** Design of interdigitated electrolytic plates. Plate finger width (w) and gap (g) are changed while the total plate area is kept constant. **(G)** Measurement of water resistance as a function of plate width and gap. Each red circle represents a data point. **(H)** Modeling of water resistance as a function of plate width and gap. G and H have the same color scale.

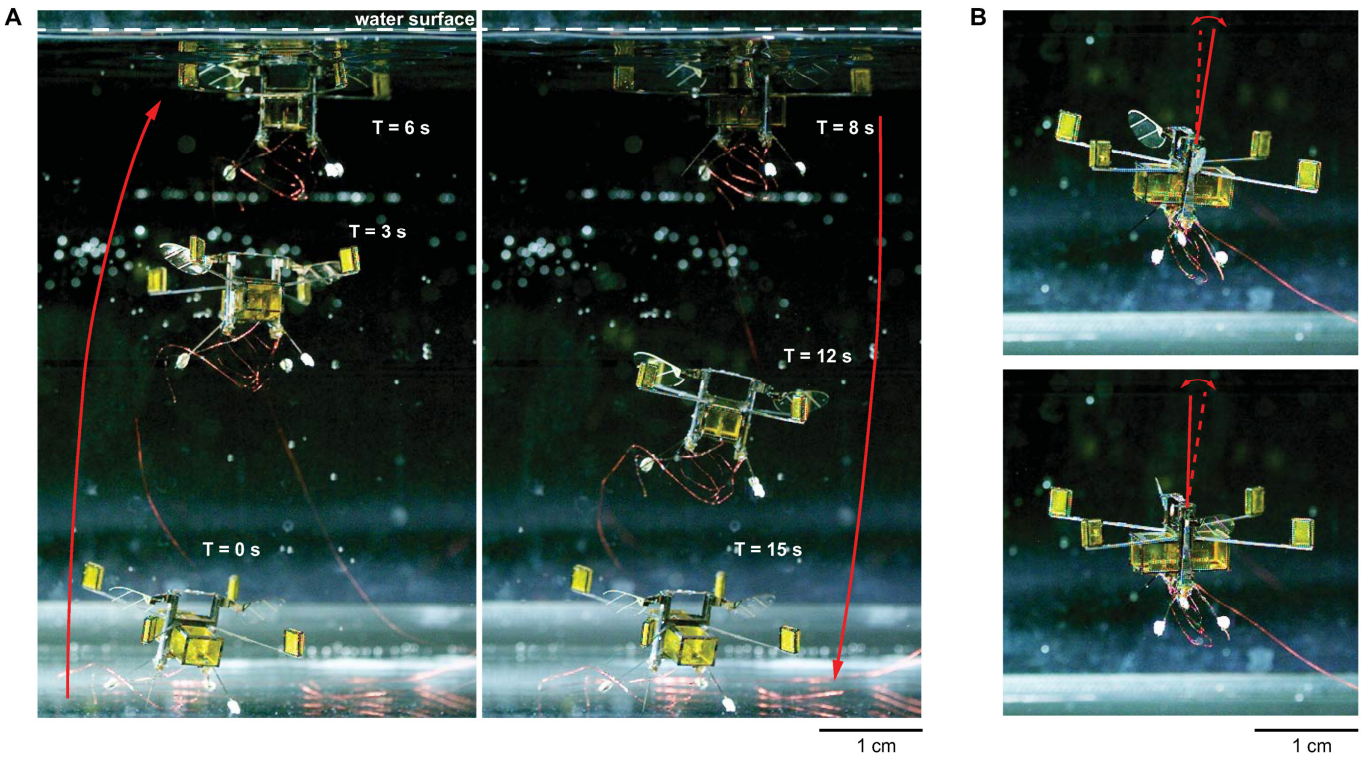

Fig. S2. Swimming demonstration of the new robot design. (A) Composite image of the robot swimming. The robot swims toward the water surface at 2 cm/s. The robot is switched off after 8 seconds and it sinks passively down to the aquarium bottom. B) Illustration of robot pitching when flapping at 9 Hz. The pitch amplitude is smaller than 5°.

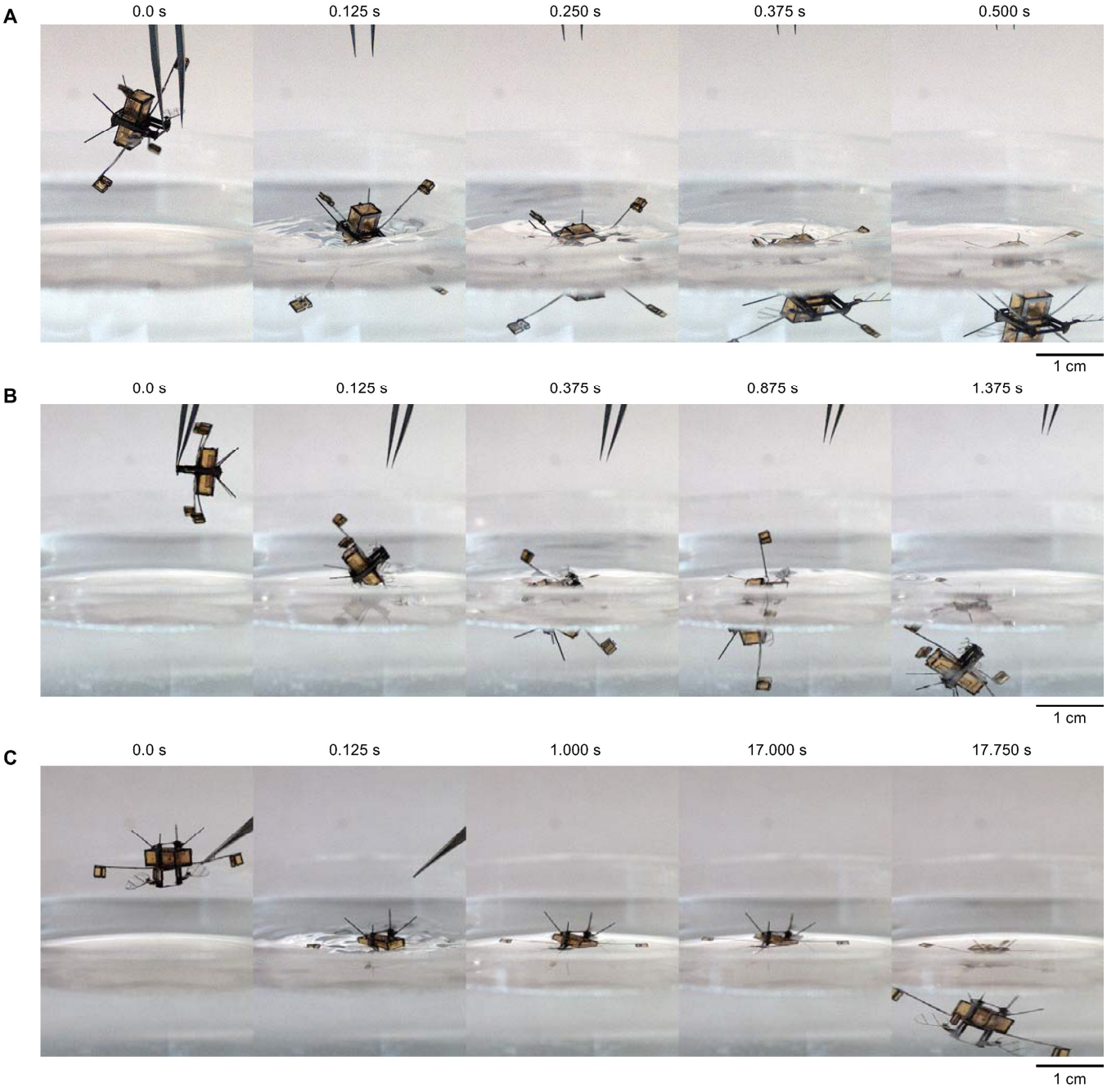

Fig. S3. Robot water entry from different orientations. (A) The robot lands on the water surface with its wings parallel to the surface. **(B)** The robot lands on the water surface with its wings at approximately 45 degree to the surface. **(C)** The robot lands on the water surface inverted. The scale bar in all images is 1 cm.

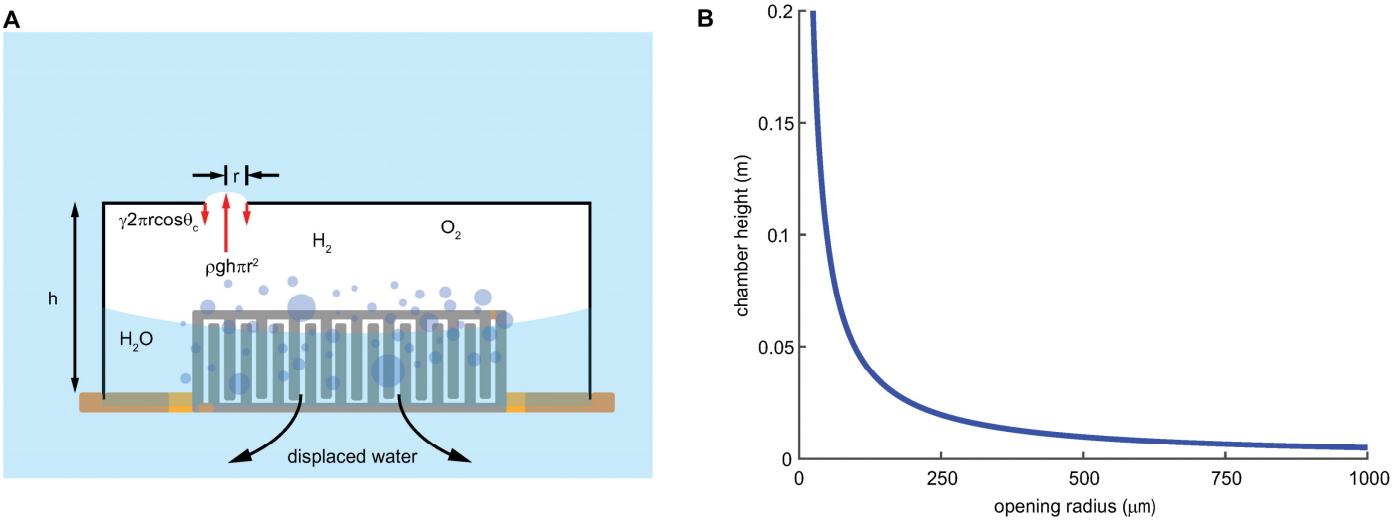

Fig. S4. Surface tension influence on height of the gas collection chamber. (A) Illustration of gas collection in a chamber with openings on the top plate. The weight of a water column of radius *r* and height *h* needs to be smaller than the surface tension force along the opening. **(B)** Maximum gas chamber height as a function of micro-opening radius.

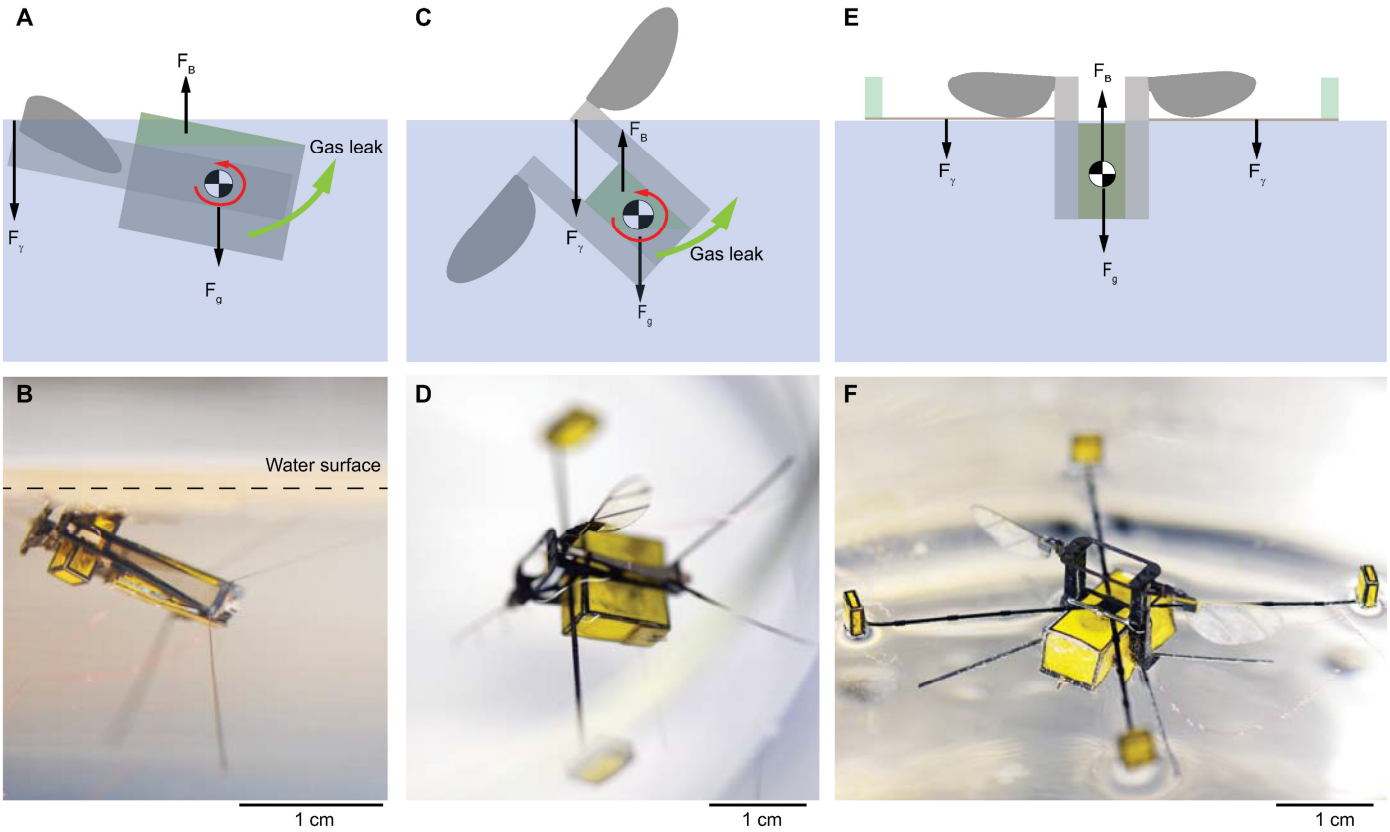

Fig. S5. Robot stability near the water surface. (A) Illustration of the robot tilted along the body pitch axis beneath the water surface. **(B)** Picture of the robot tilted along the body pitch axis. **(C)** Illustration of the robot tilted along the body roll axis after it is stabilized in the pitching axis. **(D)** Picture of the robot tilted along the body roll axis at the water surface. **(E)** Illustration of a stabilized robot with balance beams. **(F)** Picture of the robot with its wings completely emerged from the water surface.

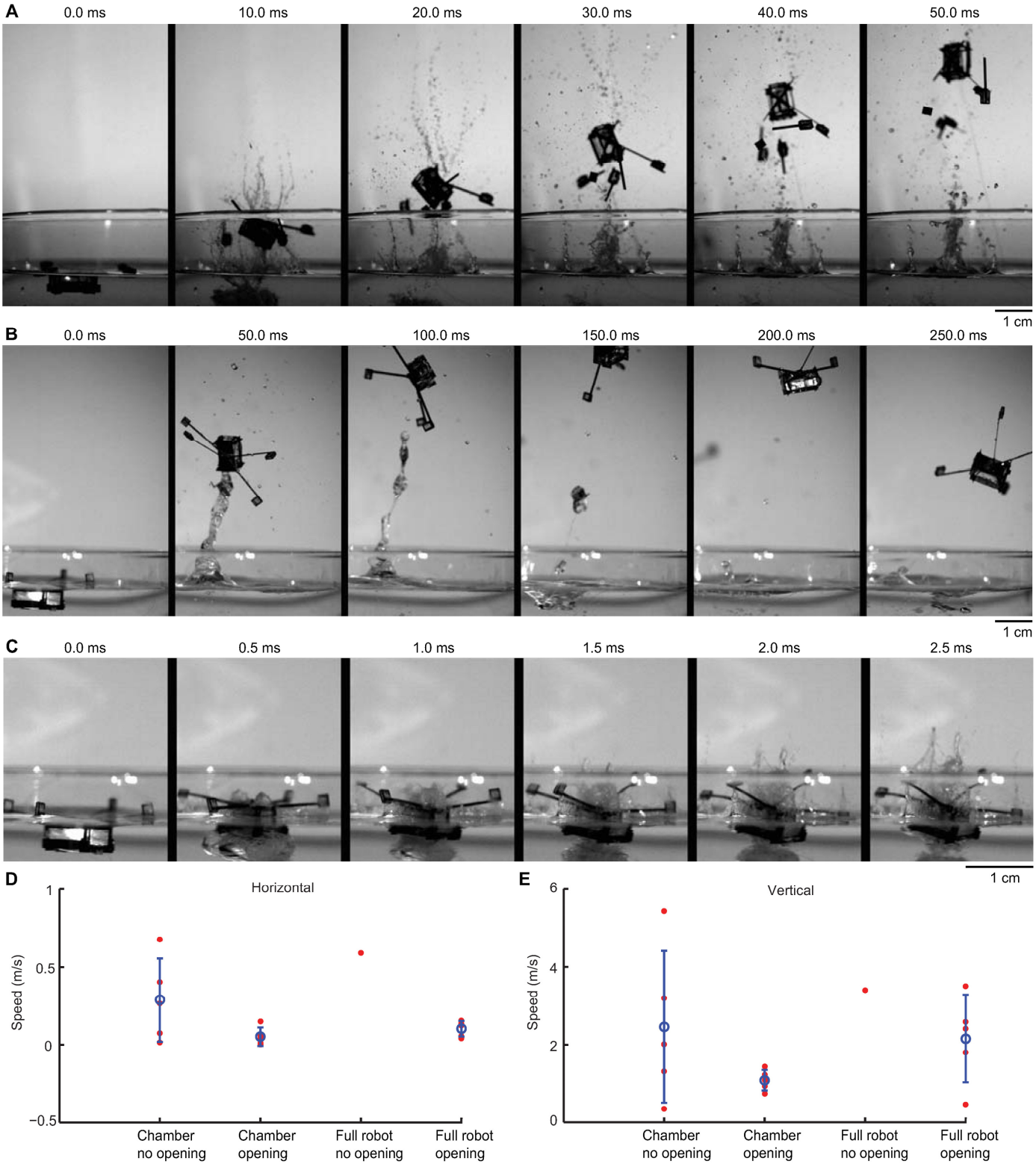

Fig. S6. Influence of micro-openings on takeoff speed. (A) Takeoff of a chamber without micro-openings. The chamber cracks open and its supporting balance beams break apart. **(B)** Takeoff of a chamber with micro-openings. **(C)** Initial takeoff images of B. Water exits the chamber through micro-openings before chamber gains momentum. **(D)** Chamber and robot takeoff speeds parallel to the water surface. **(E)** Chamber

and robot takeoff speeds perpendicular to the water surface. In D and E we report five trials for chambers with or without openings and the robot with openings. We only report one trial for the robot without openings due to damage from explosion. The blue circles and lines represent mean and standard deviation.

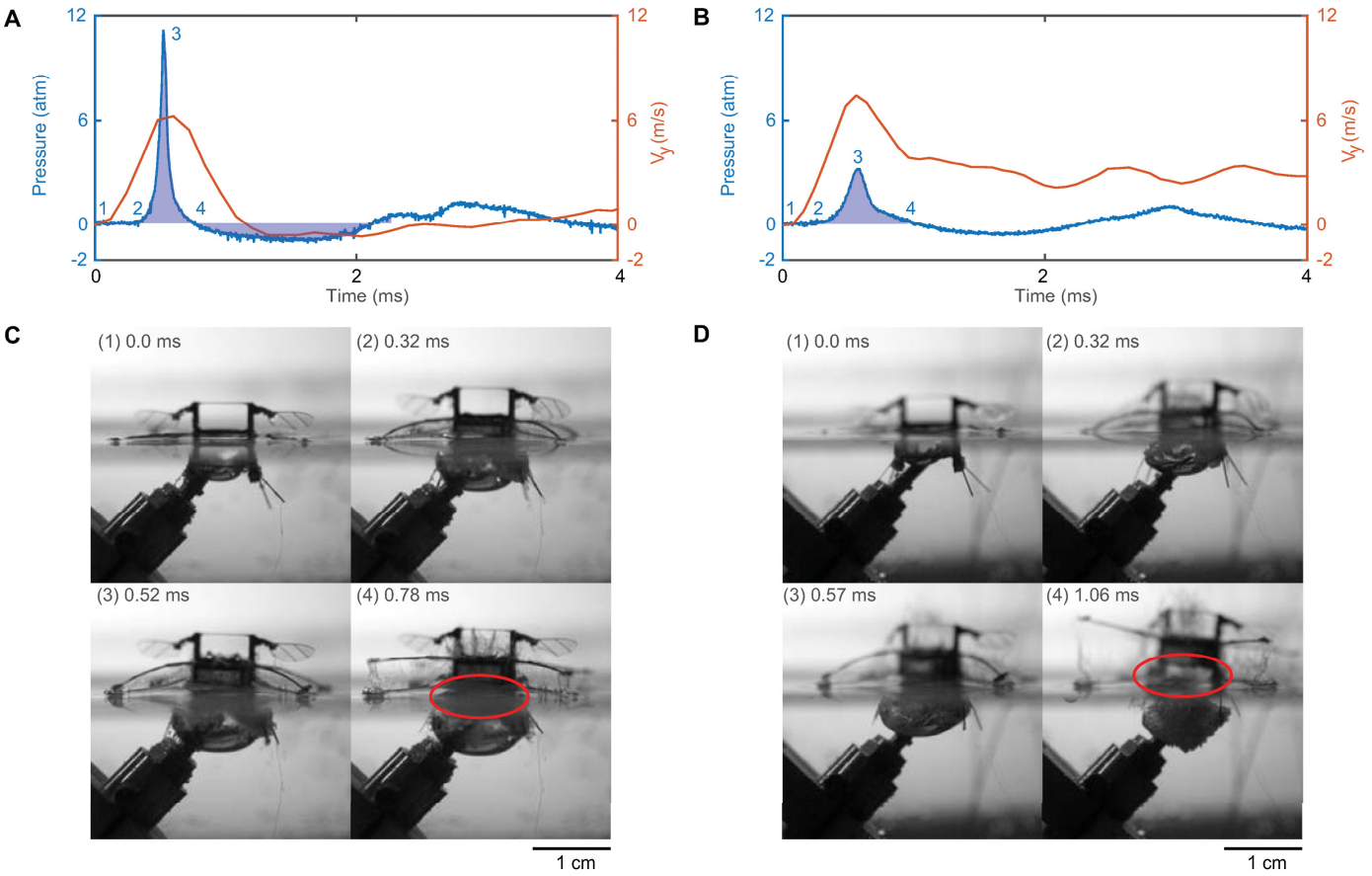

Fig. S7. Influence of micro-openings on ignition pressure and takeoff speed. (A) Pressure distribution and takeoff velocity of a robot without micro-openings. The reinforced chamber survives the explosion. **(B)** Pressure distribution and takeoff velocity of a robot with micro-openings. Shaded regions in A and B represent the net impulse before the robot exits the water. Numeric labels in A and B indicate the times of ignition (1), start of pressure rise (2), peak pressure (3), and first transition to negative pressure (4). **(C)** Image sequence of robot takeoff corresponding to numeric labels in A. The red ellipse illustrates that the chamber has not exited the water surface when ignition pressure becomes negative. **(D)** Image sequence of robot takeoff corresponding to numeric labels in B. The red ellipse illustrates that the chamber has exited the water surface when ignition pressure becomes negative.

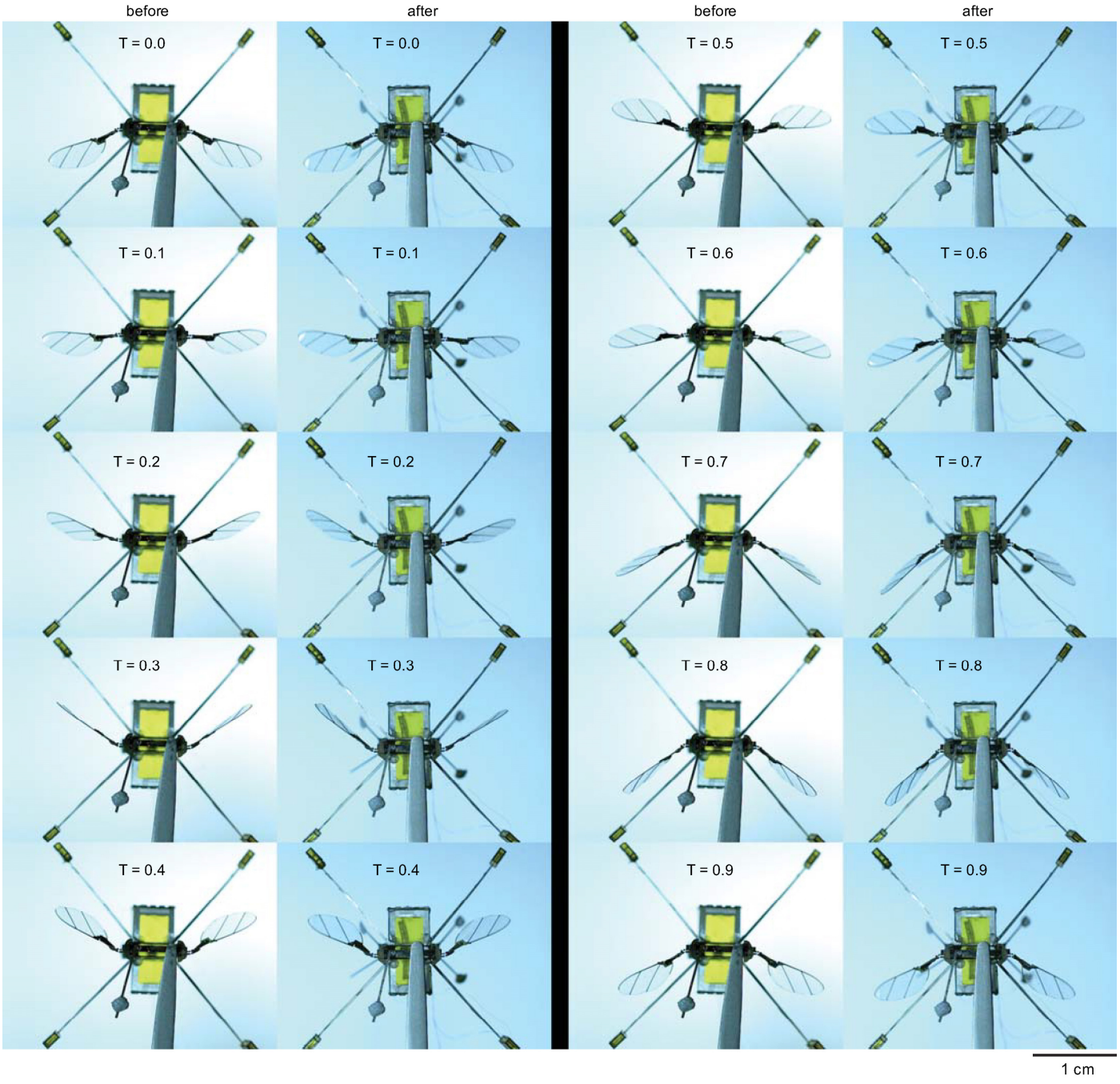

Fig. S8. Comparison of flapping kinematics before and after impulsive takeoff. The first and third columns show the robot flapping kinematics before impulsive takeoff. The second and fourth columns show the robot flapping kinematics after impulsive takeoff. The driving frequency is 265 Hz and the time scale is normalized to 1 flapping period.

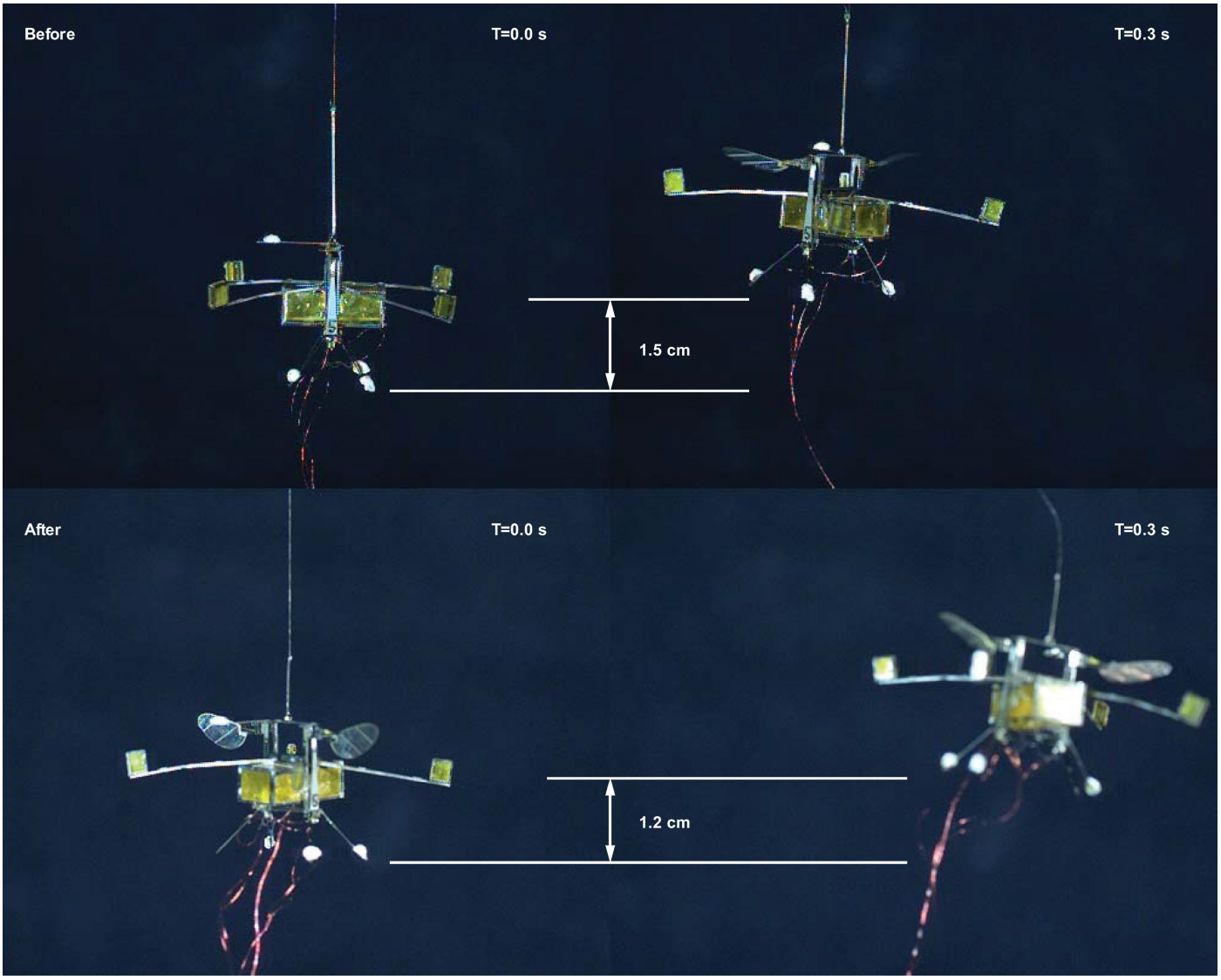

Fig. S9. Robot liftoff demonstration before and after impulsive takeoff. Before impulsive takeoff, the robot rises 1.5 cm during 0.3 seconds of test flight time. After impulsive takeoff and without any mechanical tuning, the robot rises 1.2 cm during 0.3 seconds of test flight time.

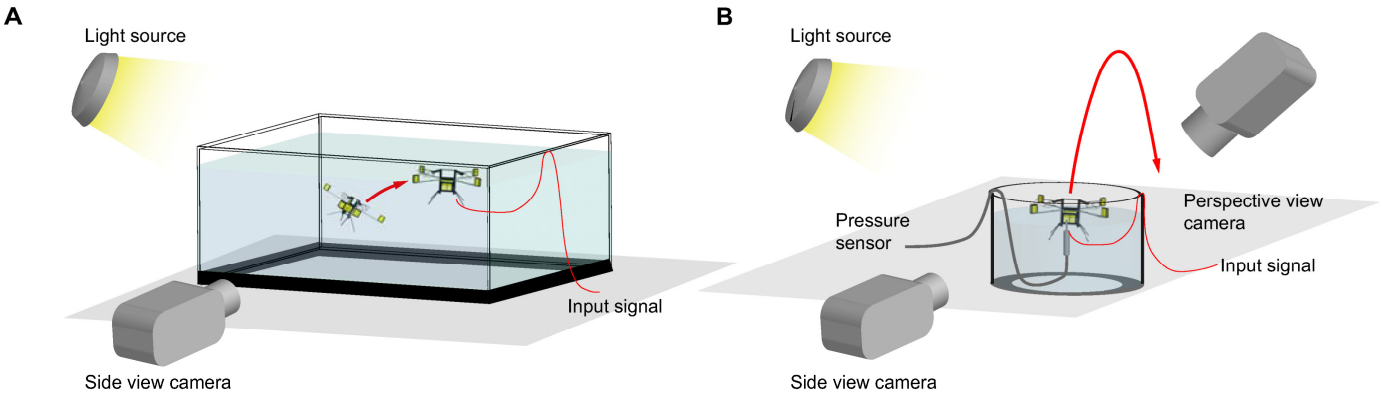

Fig. S10. Experimental setup. (A) Robot swimming experimental setup. The aquarium dimensions are 30 cm x 15 cm x 15 cm. **(B)** Robot takeoff and landing experimental setup. The aquarium radius is 7.5 cm.

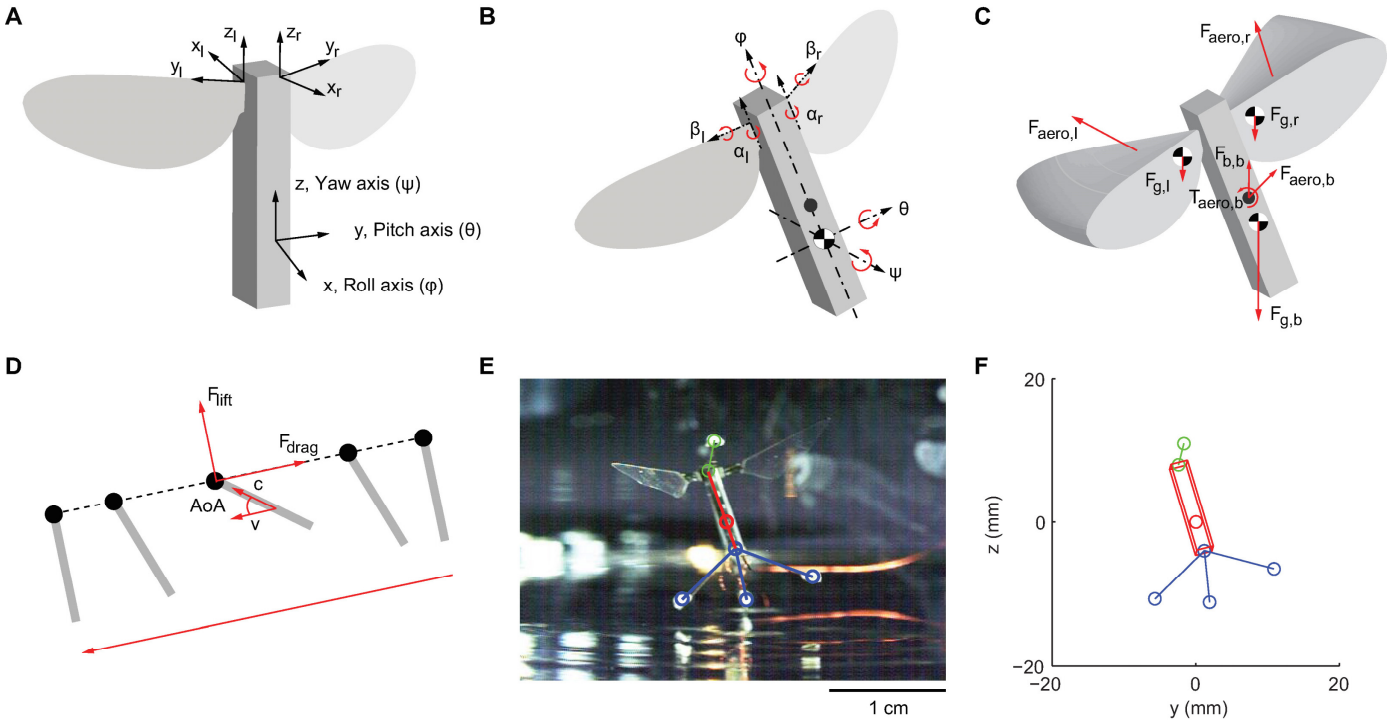

Fig. S11. Dynamical model and motion tracking method. (A) Coordinate system definition of the body, the left wing, and the right wing reference frame. **(B)** Illustration of rotational axes, robot center of mass and geometric center. **(C)** Illustration of aerodynamic forces and torques. **(D)** Definition of lift and drag directions given instantaneous stroke velocity and angle of attack. **(E)** Raw image and manual tracking of robot centroid and motion tracking markers. **(F)** Fit of the model and its projection onto the camera image plane.

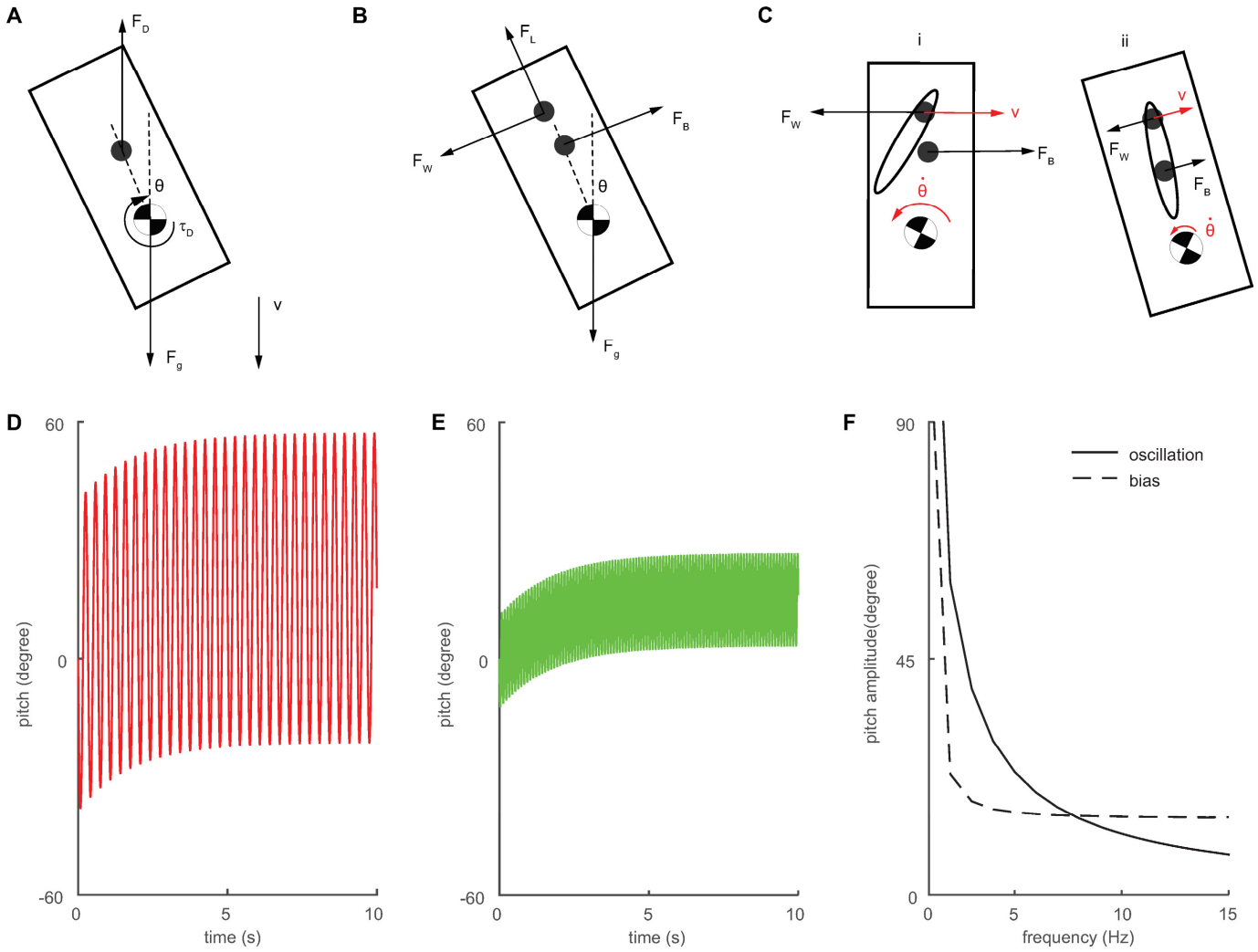

Fig. S12. Robot stability during freefall and swimming. (A) Illustration of passive upright stability during free fall when the robot center of mass is lower than its center of pressure. The aerodynamic drag force stabilizes the system. **(B)** Illustration of robot swimming stability. The drag force on the robot body (F_B) is crucial for passive stability in water. **(C)** The coupling between wing and body. C-i) The robot body has a rotational speed that is opposite to the wing stroke velocity (highlighted in red). This coupling effectively reduces the wing stroke velocity, which reduces the destabilizing drag force from the robot wing (F_W). C-ii) This coupling is the strongest during midstroke when the robot body has the largest rotational speed, and it becomes smaller as the body rotational speed is reduced at larger θ. **(D)** Simulation of body pitching when the flapping frequency is 5Hz. **(E)** Body pitching decreases a factor of three when the flapping frequency increases to 10 Hz. **(F)** Body pitch amplitude and pitch bias decrease monotonically as flapping frequency increases.

Supplementary tables

Table S1. Properties of robot components

Component name	Quantity per robot	Mass (mg)	Material	Functionality
air frame	2	15	carbon fiber	provide structural support
actuator	2	25	piezo-electric ceramic, carbon fiber, aluminum oxide	power the robot wings
transmission	2	4	carbon-fiber, polyimide	amplify actuator bending to wing flapping
wing, wing hinge	2	1	carbon-fiber, polyimide, polyester	generate propulsive forces in air or water
connection pieces	1	10	carbon fiber	affix two identical robot halves, attach other robot components
gas collection chamber	1	33	titanium, carbon fiber, polyimide	capture gas produced by electrolysis reaction chamber for detonation
sparker plate	1	6.5	copper clad FR4, stainless steel	produce oxyhydrogen by electrolysis ignite oxyhydrogen to power takeoff
balance beam	4	2	titanium	maintain robot stability on water surface; reduce body rotation during takeoff
buoyancy outriggers	4	2	carbon fiber, polyimide	increase buoyancy ; improve underwater stability
		8 - 15	Loctite 416, epoxy	Securely attach robot parts

Table S2. Model parameter values

Symbol	Parameter name	Value
A_t	top plate area	94 mm^2
A_w	wetted area	180 mm^2
μ	water viscosity	1.002 mN s / m^2
ν	water kinematic viscosity	1.004 mm^2 / s
C_D	robot drag coefficient	1
γ	soapy water surface tension coefficient	24.3 mN / m
L	balance beam length	20 mm
m	robot mass	170 mg
g	gravitational acceleration	9.8 m/s^2

Supplementary movies

Movie S1. Demonstration of robot aerial hover. The video shows hovering demonstrations of a 175 mg robot before and after impulsive takeoff. The robot flaps its wing at 265 wingbeats per second.

Movie S2. Demonstration of robot air-water transition. The video shows that surfactant lowers surface tension and facilitates robot water entry. A robot without surfactant cannot break the water surface (left). A robot coated with surfactant is dropped onto the water surface from 2 cm (center) or 10 cm (right). The robot sinks to the aquarium bottom while maintaining upright stability.

Movie S3. Demonstration of robot swimming and emergence of robot wing from the water surface. The video shows the robot swimming to the water surface and then slowly pushing out its wings by capturing the gas produced from electrolysis.

Movie S4. Demonstration of robot impulsive takeoff and landing. The video shows a robot stably lands on the ground after impulsive takeoff. Part 1 shows a zoomed-out video taken at 30 frames per second. Part 2 shows a high-speed video of the same experiment taken at 9500 frames per second.

Movie S5. Comparison of robot underwater stability with different flapping frequencies. The first part of the video compares the previous robot design operating at 5 Hz (left) versus 11 Hz (right) in water. The robot is unstable and plunges downward when operated at 5 Hz. When flapping frequency increases to 11 Hz, the robot becomes stable and swims upward to the water surface. The second part of the video shows the new robot swimming at 9 Hz. The new robot design maintains stability at its resonant flapping frequency.

Movie S6. Comparison between robot swimming experiment and simulation. The video compares experiment (left) and dynamical simulation (right) of a robot operated at 11 Hz in water. Both simulation and experiment show the robot is passively upright stable during ascent.

Movie S7. Measurement of surface tension force on a robot during water-to-air transition. The video shows a force measurement experiment as a robot is gradually pulled out of soapy water. The discontinuities of the force trace correspond to the time when robot balance beams pop out of water. The net surface tension force is given by the magnitude of these discontinuities and exceeds robot maximum lift by 2.1 times.

Movie S8. Comparison of robot takeoff with or without micro-openings on gas collection chamber. The video shows the influence of chamber micro-openings on robot takeoff. Part 1 compares the takeoff of two chambers that weigh 170 mg. The chamber without micro-openings (left) is blown into multiple pieces whereas the chamber with micro-openings (right) remains intact. Part 2 shows the side and perspective view of robot takeoff for the case of no mirco-openings. The chamber cracks open and a robot wing and balance beam are blown apart. Part 3 shows the side and perspective view of robot takeoff for the case with micro-openings. The robot experiences very small body rotation and no structural damage.

Movie S9. Detonation pressure measurement and robot takeoff. The video shows detonation pressure measurements during robot takeoff. A robot without micro-openings on its gas collection chamber (left) experiences larger detonation pressure and lower takeoff speed. The fully sealed chamber is reinforced such that it survives the detonation. A robot that has micro-openings on its gas collection chamber (right) experiences smaller detonation pressure and higher takeoff speed.